Role of Ce 4*f* hybridization in the origin of magnetism in nanoceria

V. K. Paidi,[1,*] D. L. Brewe,[2] J. W. Freeland,[2] C. A. Roberts,[3] and J. van Lierop[1,†]

[1]*Department of Physics and Astronomy, University of Manitoba, Winnipeg, Manitoba, R3T 2N2, Canada*
[2]*Advanced Photon Source, Argonne National Laboratory, Argonne, Illinois 60439, USA*
[3]*Toyota Motor Engineering and Manufacturing North America Incorporated, 1555 Woodridge Avenue,
Ann Arbor, Michigan 48105, USA*

Nanoscale CeO_2 (nanoceria) is a prototypical system that presents d^0 ferromagnetism. Using a combination of x-ray absorption spectroscopy, x-ray magnetic circular dichroism, and modeling, we show that the nanostructure, defects and disorder, and nonstoichiometry create magnetically polarized Ce 4*f* and O 2*p* hybridized states captured by the vacancy orbitals (V_{orb}) that are vital to ferromagnetism. Further, we demonstrate that foreign ions (Fe and Co) enhance the moment at Ce 4*f* sites while the number of V_{orb} is unchanged, pointing clearly to the mechanism of orbital hybridization being the key missing ingredient to understanding the unexpected ferromagnetism in many nanoscale dilute magnetic oxides and semiconductors.

Defects, disorder, and nonstoichiometry are considered to be the key ingredients for d^0 magnetism in nanoscale wide band-gap oxides. d^0 magnetism has drawn significant interest as reflected by the many reproducible experimental observations of unexpected ferromagnetism in bulk-nonmagnetic oxides such as CeO_2, ZnO, HfO_2, Al_2O_3, In_2O_3, SnO_2, and many dilute magnetic oxides [1–8]. In general, these materials have been quite puzzling due to the challenge of identifying the exact origin of the magnetism and distinguishing its spin and orbital character. It has been shown that nanoscale CeO_2 (nanoceria) is the prototypical system that has extensive spontaneous ferromagnetism with no magnetic cations [9]. The physics of this magnetism has been enigmatic. At first, the magnetism was attributed to the most obvious candidate, exchange interactions between localized electron spin moments resulting from the oxygen vacancies [1]; first-principles calculations revealed that the vacancies (especially those at the surface) can induce magnetic moments in nanoceria [10,11]. Later, the ferromagnetism was attributed to only sub-20-nm nanoceria with no obvious dependence on oxygen vacancies [12]. Others reported that mixed valence Ce^{3+}/Ce^{4+} pairs on the surface were responsible [13]. Recently, a model based on a giant orbital paramagnetism phenomenon [14] that occurs in a mesoscopic quasi-two-dimensional configuration with dilute magnetically active sites has been proposed. Despite d^0 behavior in nanoceria being widely reproducible [1,9,10,12,14–18], an understanding of the physics behind the nanomagnetism with the three key ingredients is still lacking.

In this Rapid Communication, we focus on the fundamental problem related to identifying the origin of the magnetism in nanoceria and ascertaining the mechanisms that affect the magnetic properties. We use local probes of the electronic structure and magnetism [e.g., x-ray absorption spectroscopy (XAS) and x-ray magnetic circular dichroism (XMCD), Mössbauer spectroscopy] combined with conventional magnetometry to provide insights into the underlying physics. Although there are earlier reports on the element specific magnetism of nanoceria [17–19], because of the weak XMCD signal, explicit evidence of the spin and orbital contributions to the magnetic moments of the Ce 4*f* states is still lacking. Using electronic structure, surface, and bulk magnetism measurements and simulations, we unambiguously demonstrate that vacancy orbitals (V_{orb}), Ce 4*f*–O 2*p* hybridization, and their affect on the Ce^{3+} spin and orbital angular momenta are fundamental to understanding the origins of the long-range ferromagnetic order. Additionally, we have identified that foreign ions (Fe and Co) on nanoceria enhance the ferromagnetic moment at the Ce 4*f* sites, and a microscopic mechanism is proposed to explain the origin of magnetism in nanoscale oxide semiconductors.

Nanoceria [20], and Fe- and Co-decorated nanoceria were prepared as described in Refs. [21,22]. The surface densities (chosen for no secondary phase formation) were 1.11 Fe/nm^2 and 3.57 Co/nm^2 [21,22]. X-ray diffraction (XRD) pattern refinements yielded identical CeO_2 cubic $Fm\bar{3}m$ structures for all systems [23]. Transmission electron micrographs (TEM) and high-angle annular dark-field (HAADF) images were consistent with the XRD analysis. Crystallite sizes were of the order of 20 nm in diameter and lattice constants were 5.411 ± 0.001 Å. XRD, TEM, and Mössbauer spectroscopy (see Ref. [23]) results confirmed that no secondary phases (e.g., metal oxides) were present, as do the hard and soft x-ray absorption measurements discussed below. To identify the overall magnetism, $M(\mu_0 H)$ measurements were performed [23]. The $M(\mu_0 H)$ of nanoceria shows a coercivity of $\sim$50 mT and a saturation magnetization (M_s) of $\sim$4 A m^{-1}. Co- and Fe-decorated nanoceria M_s's were $\sim$4 and 7 A m^{-1}, respectively, in agreement with many reports in the literatures (see Ref. [9] and references therein).

*paidivk@myumanitoba.ca
†Johan.van.Lierop@umanitoba.ca
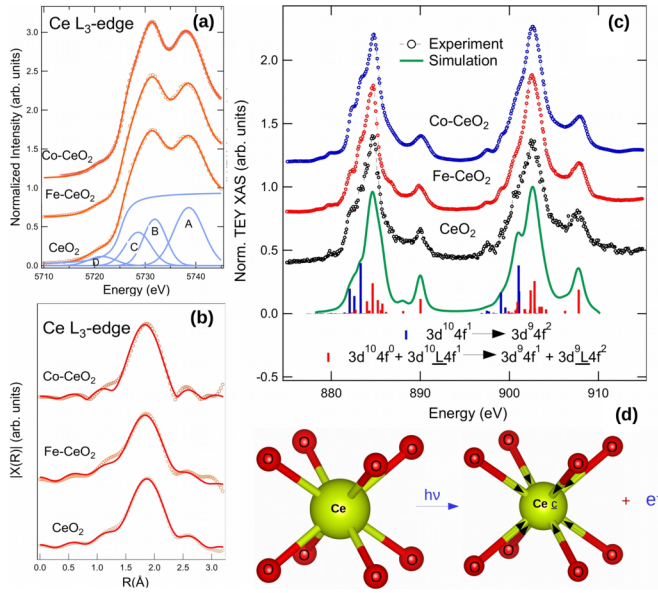
FIG. 1. (a) The normalized XANES spectra were fitted with Gaussian functions. To exclude the effects of the edge jump from fits, an arctan function was included, as shown. (b) Fourier transforms represent raw data without correcting for phase shifts. Theoretical fits are the solid lines. (c) Ce $M_{4,5}$ edge XAS data and the simulation. Charge transfer effects with $4f^0 + 4f^1\underline{L}$ ground and $4f^1 + 4f^2\underline{L}$ final states are included in order to match the experimental spectra as discussed in the text. (d) Representation of charge transfer effect between O $2p$ ligand and Ce $4f$ are shown; $\underline{c}$ is the core hole on Ce.

Because the electronic and magnetic properties of Ce ions depend strongly on the localized and delocalized $4f$ electron states, x-ray absorption near edge structure (XANES) experiments were performed to identify and quantify the oxidation state of Ce ions in nanoceria, Fe-decorated nanoceria (Fe-CeO$_2$), and Co-decorated nanoceria (Co-CeO$_2$). As shown in Fig. 1(a), XANES spectra exhibit a doublet due to the interaction between the $4f$ orbitals of the Ce atoms and $2p$ orbitals of oxygen ligands. The peculiar doublet consists of four observed peaks [24–26]. Component A is assigned to the transition from the Ce $2p$ shell to $5d$ shell (final state $2\underline{p}4f^05d^1$ with no f electrons) while component B is assigned to the excitation from the $2p$ shell to $5d$ shell along with an electron being excited from the O $2p$ shell to the Ce $4f$ shell, thus leaving a hole in the valence band (final state $2\underline{p}4f^15d^1v$; v is the hole). Component C is assigned to Ce^{3+}, and component D is assigned to the $2p_{\frac{3}{2}} \rightarrow 4f$ quadrupole transition that is a consequence of $5d$ admixtures to the $4f$ states [27]. The concentrations of Ce^{3+} from spectral weighting were estimated to be $20 \pm 2\%$. In nanoceria each Ce atom ([Xe]$4f^15d^16s^2$) can donate four electrons to bonding orbitals with two O ($1s^22s^22p^4$) atoms. When an oxygen vacancy is formed, the two electrons previously occupying p orbitals of the O atom are free to distribute. The localized electrons around Ce atoms change the oxidation state from Ce^{4+} to Ce^{3+}. The constant Ce^{3+}($4f^1$) is as expected since the Fe and Co ions are surface decorating the nanoceria (i.e., Fe and Co ions distributed randomly on the surface of the nanoceria

crystallites, bonding covalently through available O ions, as shown experimentally in Refs. [21,22]).

In order to gain insights into the local environment around Ce ions, we examined the extended x-ray absorption fine structure (EXAFS). Fourier transformed data and the corresponding EXAFS oscillations are shown in Fig. 1(b). Spectral fits identify that the bond distances of first-shell Ce-O systems are of 2.31 ± 0.04 Å. The coordination number (see Ref. [23] for details) and structural disorder around Ce (identified by Debye-Waller factors) increase in Fe-CeO$_2$ and Co-CeO$_2$. The Ce L_3 edge XAS results show that for all systems, the Ce sites exist between Ce^{3+} ($4f^1\underline{v}$) and Ce^{4+} ($4f^0$) character, with a hole ($\underline{v}$) in the O $2p$ valence band.

To describe the f electrons, their occupancy, and the electronic structure at Ce sites, we used the Ce $M_{4,5}$ edge XAS (that probes directly the valence $4f$ states by exciting electrons from $3d$ core orbitals, and gives insights into the ground state) in combination with atomic multiplet calculations based on a simplified Anderson impurity model [28,29]. The $M_{4,5}$ edge XAS spectra [Fig. 1(c)] of nanoceria consist of main peaks at 884.6 and 902.4 eV and additional weaker satellite peaks at 889.8 and 908.0 eV. The energy splitting between Ce $M_{4,5}$ edges is due to the spin-orbit coupling with the $3d_{\frac{5}{2}}$ and $3d_{\frac{3}{2}}$ core holes. The primary features of the Ce $M_{4,5}$ edge XAS spectra originate from electric-dipole allowed transitions from $3d^{10}4f^n \rightarrow 3d^94f^{n+1}$ [29]. For nanoceria, experimental spectra are simulated including Coulomb, exchange, and spin-orbit interactions by considering only $3d^{10}4f^0 \rightarrow 3d^94f^1$ and $3d^{10}4f^1 \rightarrow 3d^94f^2$ configurations. Results indicated that if we assumed only oxygen vacancies and the ground states were due to $4f^0$ and $4f^1$ atomiclike multiplets, the experimental spectra could not be modeled successfully (see Fig. S2 of Ref. [23]). In order to understand the Ce $M_{4,5}$ edge XAS spectra, especially the origin of the higher-energy satellites, we focused on the ligand hole contribution to the $3d^{10}4f^0$ ground state (from charge fluctuations in the initial and final states due to the hole on the oxygen ligand). A schematic representation of a cluster consisting of a Ce ion surrounded by eight O ions is shown in Fig. 1(d). Because of the strong Ce $4f$–O $2p$ hybridization, the initial state of the transition is described by $3d^{10}4f^0 + 3d^{10}\underline{L}4f^1$ and the final state by $3d^94f^1 + 3d^9\underline{L}4f^2$ (where $\underline{L}$ describes a hole in the O $2p$ band [30]). The two configurations in the final state form bonding ($3d^94f^1$) and antibonding ($3d^9\underline{L}4f^2$) orbital combinations. Four additional terms ΔE_{gs}, T_{gs}, ΔE_{fs}, and T_{fs} are defined to describe the relative energies and interactions of these initial and final states [29,31]. Here, $\Delta E_{\text{gs}} = E(3d^{10}\underline{L}4f^1) - E(3d^{10}4f^0)$ is the charge transfer energy between two ground states, and $T_{\text{gs}} = \langle(3d^{10}\underline{L}4f^1)|H|(3d^{10}4f^0)\rangle$ is the effective hopping integral connecting the two ground-state configurations. Similarly, $\Delta E_{\text{fs}} = E(3d^9\underline{L}4f^2) - E(3d^94f^1)$ and $T_{\text{fs}} = \langle(3d^9\underline{L}4f^2)|H|(3d^94f^1)\rangle$ are charge transfer and hopping integrals of the final state [23]. Our simulation was modeled with 77% $3d^{10}4f^0$ and 23% $3d^{10}\underline{L}4f^1$ ground-state configurations and $\Delta E_{\text{gs}} = 2.0$ eV and $T_{\text{gs}} = 0.77$ eV. The ΔE_{fs} is defined as the sum of $\Delta E_{\text{gs}} + U_{ff} - U_{fd}$, where U_{ff} represent the Coulomb repulsion and U_{fd} the core-valence repulsion integrals. Our simulation agrees best with the experimental data with $\Delta E_{\text{fs}} = -2.5$ eV. For a purely Ce^{4+}-based system, the Ce $M_{4,5}$ edge $\Delta E_{\text{fs}} = -1.5$ eV [32]. In lanthanides it is

expected that $U_{ff} > U_{fd}$ due to the smaller orbital radius [28]. However, in nanoceria, $U_{fd} > U_{ff}$ indicates that the charge transfer energy is reduced due to covalent Ce $4f$–O $2p$ states in this mixed valency system. Earlier, on the basis of band-structure calculations, it was shown that ceria is less ionic [33].

Covalent orbitals play a major role in understanding the origin of magnetism. In trivalent Ce compounds such as $CeRh_3B_2$ and CeCuSi the magnetism is due to highly localized $4f$ electrons. By contrast in tetravalent α-cerium compounds $CeFe_2$ or $CeCo_5$, the magnetism is from hybridization between $4f$ and conduction electrons [34]. The results of density functional theory calculations local density approximation (LDA+U), local spin density approximation (LSDA)+U, LDA/generalized gradient approxmation (GGA)+U of nanoceria are controversial. Some studies support charge localization in the oxygen vacancies [10,11] as the source of the magnetism. Other studies identify Ce vacancies [35,36] as responsible for ferromagnetism (via superexchange between localized electrons in vacancies and neighboring Ce sites). Finally, some challenge both arguments [37], leaving the question unresolved. Identifying the origin of magnetism in nanoceria (via bulk magnetization techniques such as magnetometry and susceptometry) is complex due to the challenges in decoupling the contributions from Ce mixed valence states and oxygen vacancies. X-ray magnetic circular dichroism (XMCD) is a sensitive tool to investigate the source of magnetism at an elemental atomic level via the excitation of core level electrons to unoccupied states above the Fermi level (E_F). XMCD experiments have the advantage of being site and orbital selective due to the electric (or quadrupole) selection rules. To gain insights into the role of the $4f$ electrons' contribution (conduction or hybridized), we performed surface and bulk sensitive XMCD measurements simultaneously using total electron yield (TEY) and total fluorescence yield (TFY) over the $M_{4,5}$ edges; TEY probes the first ∼2 nm of the surface while TFY measures the complete sample but is prone to self-absorption effects [38]. In Fig. 2 we present the 10-K artifact-free [39] ±5 T XMCD spectra. The TEY Co-CeO_2 Ce $M_{5,4}$ XMCD in Fig. 2(a) is the most representative due to the least amount of surface charging. Note that ceria is a poor conductor, and Co-CeO_2's conductivity is high compared to that of Fe-CeO_2 and CeO_2, which made it difficult to measure a clean XMCD spectra in TEY for the Fe and CeO_2 samples. Both TEY and TFY XMCD spectra clearly identify that the Ce $4f$ electrons unambiguously carry a magnetic moment on both the surface and in the bulk.

To quantify the magnetic moment, XMCD spectra were simulated using XCLAIM [40] for the $3d^{10}4f^1 \rightarrow 3d^9 4f^2$ transition in the atomic limit. The contributions of the XMCD spectral orbital and spin magnetic moments obtained from the surface and bulk contributions are given in Table I. This dichroic signal is explicit evidence of Ce sites carrying magnetizable moments. In general, the spectral shapes of the Ce $M_{4,5}$ edges are indicative of a ground-state total angular momentum ($J = \frac{5}{2}$ for a pure state $4f^1$ state). Any changes in the XMCD spectral shape can be attributed to different values of J contributing to the ground state [34,41]. It is important to note that the simulated spectra for a pure $J = \frac{5}{2}$ state are not in complete agreement with experiment [e.g.,
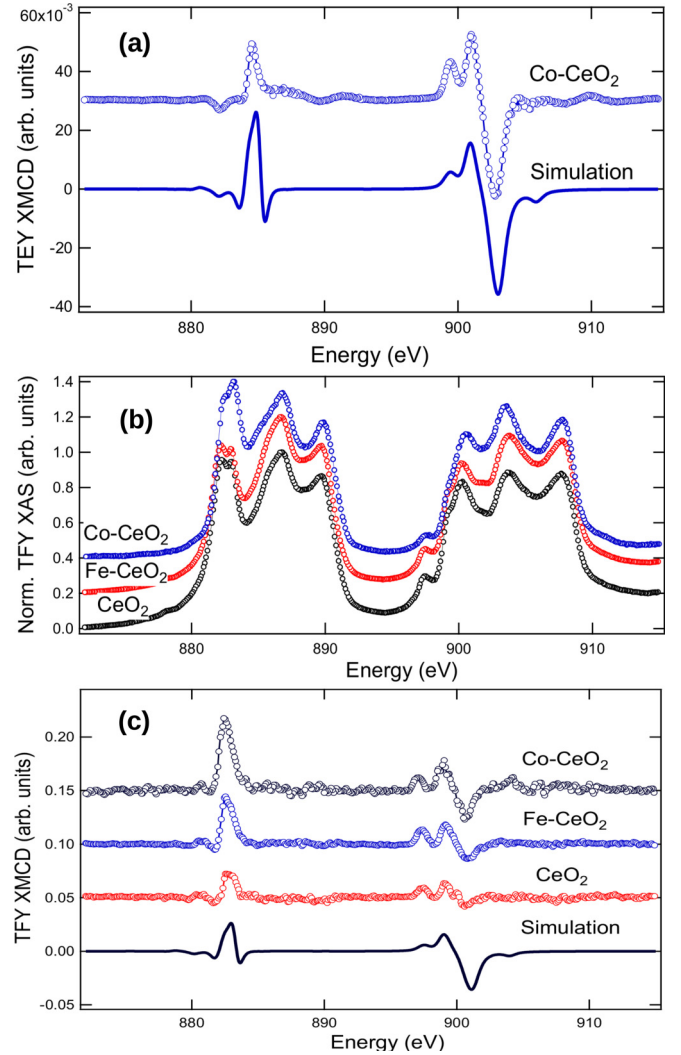
FIG. 2. Ce $M_{4,5}$ TEY (surface) and TFY (bulk) XMCD spectra evidencing the magnetic moment at Ce $4f$ sites. (a) Co-CeO_2 TEY XMCD and simulation are shown. (b), (c) A comparison of Ce $M_{4,5}$ XAS and XMCD is shown. The origin of the energy axis of the simulated spectra has been chosen to align with the maximum intensity peak of the M_5 edge and the simulated spectra is reduced by a factor of 12 to match the experimental intensity of nanoceria.

Fig. 2(a), a negative peak present at the M_5 edge and an overestimation(underestimation) of M_5 (M_4) dichroic signals]. Interestingly, nanoceria's Ce $M_{4,5}$ XMCD spectral line shape

TABLE I. Contributions of the z component of the orbital and spin magnetic moments obtained from the TEY (surface) XMCD simulations of Co-CeO_2 and TFY (bulk) XMCD of CeO_2, Fe-CeO_2, and Co-CeO_2 nanocrystallites.

	Co-CeO_2 TEY/surface	CeO_2 TFY	Fe-CeO_2 TFY	Co-CeO_2 TFY
$\langle L_z \rangle (\hbar)$	−0.24(1)	−0.24(1)	−0.36(2)	−0.48(2)
$\langle S_z \rangle (\hbar)$	0.03(1)	0.03(1)	0.05(1)	0.06(2)
$\langle J_z \rangle (\hbar)$	−0.21(1)	−0.21(1)	−0.32(2)	−0.42(2)
$\langle L_z \rangle / \langle S_z \rangle$	−8	−8	−7	−8

is different from $CeRh_3B_2$ and $CeCuSi$ [34] (where the ground state is pure $J = \frac{5}{2}$ and magnetism is due to $4f$ conduction electrons) but quite similar to the XMCD spectra of $CeFe_2$ and a Ce/Fe multilayer (the ground state is a mixture of $J = \frac{5}{2}$ and $J = \frac{7}{2}$ [34,42]). This is indicative of Ce $4f$ electrons being strongly hybridized with the O $2p$ valence band. At the M edges, although the TFY XAS signal is distorted [43] because of self-absorption [Fig. 2(b)], the TFY XMCD [Fig. 2(c)] signal is similar to TEY XMCD (surface). The TFY XMCD magnitude increases in the order of CeO_2 < Fe-CeO_2 < Co-CeO_2. Results identify that foreign ions with intrinsic moments (such as Fe and Co) enhances [23] the overall Ce magnetic moment (Fig. 2(c) and Table I).

XMCD measurements (atomic magnetism) identify the average magnetic moment as $0.18\mu_B$/Ce [23], and if all Ce $4f$ magnetic states are contributing to the ferromagnetism, the ∼20-nm CeO_2 crystallites are expected to show ∼$2000\mu_B$/crystallite. In contrast, superconducting quantum interference device (SQUID) magnetometry measures the magnetization from the Ce $4f$, V_{orb}, and hybridization contributions with $M_s = 2\mu_B$/crystallite identifying that the ferromagnetic volume fraction is only 0.1% (see Ref. [23] for XMCD and SQUID magnetometry moment calculations). Clearly, not all Ce $4f$ states are involved in the magnetism; only the fraction associated with the V_{orb} and/or hybridization (it follows that because of the low fraction, only Ce $4f$–O $2p$ hybridized states that are captured in the delocalized V_{orb} are associated) are responsible.

The radial extent of Ce $4f$ orbitals [44] is very small (0.54 Å) and that limits the Ce $4f$–O $2p$ covalent mixing to be relatively low as supported by various DFT/LDA/GGA calculations [45]. However, the size (0.5–0.8 nm diameter) of the V_{orb} is large (see Ref. [23] for the calculation) and less localized compared to the Ce $4f$ states. This is consistent with first-principles calculations that found the size of V_{orb} at ∼1.0 nm [46]. Note that only the trapped Ce $4f$ states in the V_{orb} can polarize spin moments (due to their delocalized nature) on the hybridized states and be responsible for the long-range ferromagnetic order. The residual $4f$ states that are not in the vicinity of V_{orb} cannot contribute to the ferromagnetism due to the lack of hybridized magnetic states. If the number of V_{orb} is constant, introducing foreign transition-metal ions (Fe or Co) impacts Ce $4f$–O $2p$ hybridization and further promotes a robust, yet weak, ferromagnetism. Figure 3 shows the illustration of this microscopic model. This description is consistent with the observation that air or O_2 annealed d^0 nanoscale magnetic oxides exhibit reduced or annihilated magnetism [1,9,47], as O_2 fills the vacancies resulting in a deficiency of V_{orb} coupling channels.
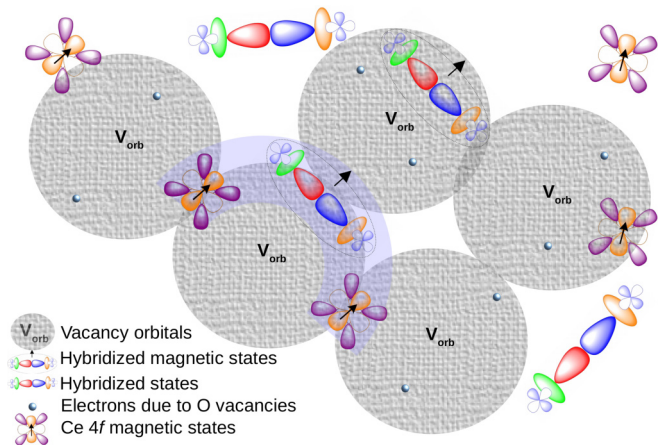
FIG. 3. Graphical illustration of the magnetic model. Ce $4f$ magnetic states, V_{orb}, and hybridized Ce $4f$ and O $2p$ states are shown. Ce $4f$ states captured in the V_{orb} polarize the hybridized states and provide a channel to mediate the ferromagnetism. The shaded region illustrates the magnetic exchange process as discussed in the text.

In summary, we have found a possible pathway to explain the origin of ferromagnetism in the dilute magnetic oxide nanoceria. Using a combination of electronic structure, elemental, and bulk sensitive magnetism techniques, we show that V_{orb}, Ce $4f$ spin and orbital angular momentum, and hybridization with O $2p$ states are crucial for the magnetic ordering. The concept of magnetism from hybridized Ce $4f$–O $2p$ states in trapped V_{orb} is a missing link to understand the ferromagnetism in nanoceria. In closing, this work provides unambiguous experimental evidence of the origin of ferromagnetism in nanoceria, and demonstrates that this hybridization concept may be a solid foundation from which to explain the unexpected ferromagnetism in ZnO, HfO_2, Al_2O_3, In_2O_3, SnO_2, and many other dilute magnetic oxides and semiconductors (where O $2p$ hole states are key players, and their hybridization with host or guest metal ions changes the density of states) that present similar magnetism.

[1] A. Sundaresan, R. Bhargavi, N. Rangarajan, U. Siddesh, and C. N. R. Rao, Phys. Rev. B **74**, 161306(R) (2006).

[2] B. B. Straumal, A. A. Mazilkin, S. G. Protasova, A. A. Myatiev, P. B. Straumal, G. Schütz, P. A. van Aken, E. Goering, and B. Baretzky, Phys. Rev. B **79**, 205206 (2009).

[3] J. Chaboy, R. Boada, C. Piquer, M. A. Laguna-Marco, M. García-Hernández, N. Carmona, J. Llopis, M. L. Ruíz-González, J. González-Calbet, J. F. Fernández, and M. A. García, Phys. Rev. B **82**, 064411 (2010).

[4] A. S. Esmaeily, M. Venkatesan, S. Sen, and J. M. D. Coey, Phys. Rev. Mater. **2**, 054405 (2018).

[5] J. M. D. Coey, Solid State Sci. **7**, 660 (2005).

[6] J. M. D. Coey and S. Chambers, MRS Bull. **33**, 1053 (2008).

[7] T. Dietl, Nat. Mater. **9**, 965 (2010).

[8] R. J. Green, T. Z. Regier, B. Leedahl, J. A. McLeod, X. H. Xu, G. S. Chang, E. Z. Kurmaev, and A. Moewes, Phys. Rev. Lett. **115**, 167401 (2015).

[9] K. Ackland and J. M. D. Coey, Phys. Rep. **746**, 1 (2018).

[10] M. Ge, H. Wang, E. Liu, J. Liu, J. Jiang, Y. Li, Z. Xu, and H. Li, Appl. Phys. Lett. **93**, 062505 (2008).

[11] X. Han, J. Lee, and H.-I. Yoo, Phys. Rev. B **79**, 100403(R) (2009).

[12] Y. Liu, Z. Lockman, A. Aziz, and J. MacManus-Driscoll, J. Phys.: Condens. Matter **20**, 165201 (2008).

[13] M. Li, S. Ge, W. Qiao, L. Zhang, Y. Zuo, and S. Yan, Appl. Phys. Lett. **94**, 152511 (2009).

[14] M. Coey, K. Ackland, M. Venkatesan, and S. Sen, Nat. Phys. **12**, 694 (2016).

[15] N. Paunović, Z. Dohčević-Mitrović, R. Scurtu, S. Aškrabić, M. Prekajski, B. Matović, and Z. V. Popović, Nanoscale **4**, 5469 (2012).

[16] K. Ackland, L. M. A. Monzon, M. Venkatesan, and J. M. D. Coey, IEEE Trans. Magn. **47**, 3509 (2011).

[17] S.-Y. Chen, C.-H. Tsai, M.-Z. Huang, D.-C. Yan, T.-W. Huang, A. Gloter, C.-L. Chen, H.-J. Lin, C.-T. Chen, and C.-L. Dong, J. Phys. Chem. C **116**, 8707 (2012).

[18] W. Lee, S.-Y. Chen, Y.-S. Chen, C.-L. Dong, H.-J. Lin, C.-T. Chen, and A. Gloter, J. Phys. Chem. C **118**, 26359 (2014).

[19] D.-Z. Peng, S.-Y. Chen, C.-L. Chen, A. Gloter, F.-T. Huang, C.-L. Dong, T.-S. Chan, J.-M. Chen, J.-F. Lee, H.-J. Lin *et al.*, Langmuir **30**, 10430 (2014).

[20] C. I. Kasei Co., Ltd., NanoTek powder.

[21] C. A. Roberts, D. Prieto-Centurion, Y. Nagai, Y. F. Nishimura, R. D. Desautels, J. van Lierop, P. T. Fanson, and J. M. Notestein, J. Phys. Chem. C **119**, 4224 (2015).

[22] T. C. Peck, G. K. Reddy, M. Jones, and C. A. Roberts, J. Phys. Chem. C **121**, 8435 (2017).

[23] See Supplemental Material at http://link.aps.org/supplemental/10.1103/PhysRevB.99.180403 for details of XRD, TEM, HAADF, Brunauer–Emmett–Teller (BET) analysis, inductively coupled plasma (ICP) spectroscopy, XAS simulations, XAFS analysis, SQUID magnetometry, and V_{orb} calculations.

[24] H. Dexpert, R. C. Karnatak, J.-M. Esteva, J. P. Connerade, M. Gasgnier, P. E. Caro, and L. Albert, Phys. Rev. B **36**, 1750 (1987).

[25] G. Kaindl, G. Schmiester, E. V. Sampathkumaran, and P. Wachter, Phys. Rev. B **38**, 10174 (1988).

[26] A. V. Soldatov, T. S. Ivanchenko, S. Della Longa, A. Kotani, Y. Iwamoto, and A. Bianconi, Phys. Rev. B **50**, 5074 (1994).

[27] T. K. Sham, R. A. Gordon, and S. M. Heald, Phys. Rev. B **72**, 035113 (2005).

[28] F. de Groot, Coord. Chem. Rev. **249**, 31 (2005).

[29] B. T. Thole, G. van der Laan, J. C. Fuggle, G. A. Sawatzky, R. C. Karnatak, and J.-M. Esteva, Phys. Rev. B **32**, 5107 (1985).

[30] S. M. Butorin, D. C. Mancini, J.-H. Guo, N. Wassdahl, J. Nordgren, M. Nakazawa, S. Tanaka, T. Uozumi, A. Kotani, Y. Ma, K. E. Myano, B. A. Karlin, and D. K. Shuh, Phys. Rev. Lett. **77**, 574 (1996).

[31] R. D. Cowan, *The Theory of Atomic Structure and Spectra*, 3 (University of California Press, Berkeley, CA, 1981).

[32] M. W. Loöble, J. M. Keith, A. B. Altman, S. C. E. Stieber, E. R. Batista, K. S. Boland, S. D. Conradson, D. L. Clark, J. Lezama Pacheco, S. A. Kozimor *et al.*, J. Am. Chem. Soc. **137**, 2506 (2015).

[33] D. Koelling, A. Boring, and J. Wood, Solid State Commun. **47**, 227 (1983).

[34] J. P. Schillé, F. Bertran, M. Finazzi, C. Brouder, J. P. Kappler, and G. Krill, Phys. Rev. B **50**, 2985 (1994).

[35] V. Fernandes, R. J. O. Mossanek, P. Schio, J. J. Klein, A. J. A. de Oliveira, W. A. Ortiz, N. Mattoso, J. Varalda, W. H. Schreiner, M. Abbate, and D. H. Mosca, Phys. Rev. B **80**, 035202 (2009).

[36] L. Zhan-Sheng, M. Dong-Wei, Z. Jing, X. Guo-Liang, and Y. Zong-Xian, Chin. Phys. B **21**, 047505 (2012).

[37] P. Keating, D. Scanlon, and G. Watson, J. Phys.: Condens. Matter **21**, 405502 (2009).

[38] W. T. Fuhrman, J. C. Leiner, J. W. Freeland, M. van Veenendaal, S. M. Koohpayeh, W. A. Phelan, T. M. McQueen, and C. Broholm, Phys. Rev. B **99**, 020401(R) (2019).

[39] The XMCD spectra were obtained as the difference of the corrected x-ray absorption spectra for both left and right circularly polarizations. To make sure that the final XMCD spectra were free of experimental artifacts, such as those from charging effects, spectra were also collected for the opposite applied field direction.

[40] J. Fernández-Rodríguez, B. Toby, and M. van Veenendaal, J. Electron Spectrosc. Relat. Phenom. **202**, 81 (2015).

[41] G. van der Laan, B. Thole, G. Sawatzky, J. Fuggle, and R. Karnatak, J. Phys. C **19**, 817 (1986).

[42] M. Finazzi, F. M. F. de Groot, A.-M. Dias, B. Kierren, F. Bertran, P. Sainctavit, J.-P. Kappler, O. Schulte, W. Felsch, and G. Krill, Phys. Rev. Lett. **75**, 4654 (1995).

[43] S. Butorin, D. Mancini, J.-H. Guo, N. Wassdahl, and J. Nordgren, J. Alloys Compd. **225**, 230 (1995).

[44] Z. Barandiarán and L. Seijo, J. Chem. Phys. **119**, 3785 (2003).

[45] J. Paier, C. Penschke, and J. Sauer, Chem. Rev. **113**, 3949 (2013).

[46] T. S. Herng, D.-C. Qi, T. Berlijn, J. B. Yi, K. S. Yang, Y. Dai, Y. P. Feng, I. Santoso, C. Sánchez-Hanke, X. Y. Gao, A. T. S. Wee, W. Ku, J. Ding, and A. Rusydi, Phys. Rev. Lett. **105**, 207201 (2010).

[47] N. H. Hong, N. Poirot, and J. Sakai, Appl. Phys. Lett. **89**, 042503 (2006).